Shock-induced formation of wüstite and fayalite in a magnetite-quartz target rock

Leonard F. HENRICHS [1,2], Agnes KONTNY[2*], Boris REZNIK[2], Uta GERHARDS[3],
Jörg GÖTTLICHER[4], Tim GENSSLE[2], and Frank SCHILLING[2]

[1]Karlsruhe Institute of Technology, Institute of Nanotechnology, Hermann-von-Helmholtz-Platz 1,
76344 Eggenstein-Leopoldshafen, Germany
[2]Karlsruhe Institute of Technology, Institute of Applied Geosciences, Adenauerring 20, 76131 Karlsruhe, Germany
[3]Karlsruhe Institute of Technology, Institute for Micro Process Engineering, Hermann-von-Helmholtz-Platz 1,
76344 Eggenstein-Leopoldshafen, Germany
[4]Karlsruhe Institute of Technology, Institute for Photon Science and Synchrotron Radiation (IPS),
Hermann-von-Helmholtz-Platz 1, 76344 Eggenstein-Leopoldshafen, Germany
[*]Corresponding author. E-mail: agnes.kontny@kit.edu

Abstract–Projectile–target interactions as a result of a large bolide impact are important issues, as abundant extraterrestrial material has been delivered to the Earth throughout its history. Here, we report results of shock-recovery experiments with a magnetite-quartz target rock positioned in an ARMCO iron container. Petrography, synchrotron-assisted X-ray powder diffraction, and micro-chemical analysis confirm the appearance of wüstite, fayalite, and iron in targets subjected to 30 GPa. The newly formed mineral phases occur along shock veins and melt pockets within the magnetite-quartz aggregates, as well as along intergranular fractures. We suggest that iron melt formed locally at the contact between ARMCO container and target, and intruded the sample causing melt corrosion at the rims of intensely fractured magnetite and quartz. The strongly reducing iron melt, in the form of μm-sized droplets, caused mainly a diffusion rim of wüstite with minor melt corrosion around magnetite. In contact with quartz, iron reacted to form an iron-enriched silicate melt, from which fayalite crystallized rapidly as dendritic grains. The temperatures required for these transformations are estimated between 1200 and 1600 °C, indicating extreme local temperature spikes during the 30 GPa shock pressure experiments.

INTRODUCTION

Hypervelocity impact events are local but widespread phenomena in our solar system, leading to enormous petrological and mineralogical changes in rocks. Correspondingly, it is an important scientific challenge to reveal impact-related microstructural changes occurring in rocks. Frequently, magnetic anomalies accompany impact structures (e.g., Pilkington and Grieve 1992; Acuna et al. 1999). Understanding the effect of shock waves on magnetic and structural properties of magnetite (Fe_3O_4) as one of the most abundant magnetic carriers in impacted rocks is an important objective (e.g., Gattacceca et al. 2007).

Our recent investigations of a laboratory-shocked magnetite-quartz ore demonstrate that increasing shock pressure causes variations in magnetic and structural properties of magnetite (Reznik et al. 2016a), as well as structural modifications in quartz, biotite, and amphibole (Reznik et al. 2016b). However, possible structural and phase transformations occurring at the interfacial regions between minerals like magnetite and quartz were not within the scope of our previous studies (Reznik et al. 2016a, 2016b; Kontny et al. 2018), and we did not concentrate on interactions between the ARMCO iron container and the target rock.

Interactions of projectiles with target rocks are reported from natural impactites, such as Henbury crater in Australia (Ding and Veblen 2004), the Wabar craters in Saudi Arabia (Hamann et al. 2013), or Kamil crater in Egypt (D'Orazio et al. 2011). In all

these craters, an iron meteorite impacted a silicate-rich sedimentary target rock and metallic and silicate melts were produced. During the mixing process, projectile droplets and target melts underwent significant chemical changes, and cooling of these mixtures induced liquid immiscibilities and phase separations of different melts under supercooled and reducing conditions. Kowitz et al. (2013) and Ebert et al. (2018) showed that significant mechanical and chemical mixing processes also occur during shock-recovery experiments with sandstone around 10 GPa. In these experiments, high explosives were used to accelerate a driver plate onto the ARMCO iron container enclosing the target rock. Most prominent is an injection of ARMCO iron melt into the silicate melts formed in the target.

Our study presents phase transformations and melting processes, observed locally in a magnetite-quartz target subjected to shock waves. We demonstrate that after applying a sufficiently high mechanical shock of 30 GPa, the magnetite-quartz ore reacts with the ARMCO iron and formed wüstite (FeO) and fayalite (Fe_2SiO_4) containing iron droplets. This observation has far-reaching implications for a better understanding of projectile–target interactions on the Earth and other planetary bodies and their magnetic properties.

MATERIALS AND METHODS

Shock-recovery experiments were performed at the Ernst Mach Institute, Freiburg, Germany, using a high-explosive setup described in detail elsewhere (e.g., Langenhorst and Hornemann 2005; Reznik et al. 2016a). The target material was a dense, pore-free quartz-magnetite banded iron ore with traces of hornblende and pyrite from the Sydvaranger mine, Finnmark/Norway. A 15 mm diameter ore disc with a thickness of about 1.3 mm has been placed into the ARMCO iron container (Figs. 1a and 1b). The free distance between flyer plate and target surface was set by an acrylic glass spacer ring. High explosives were used to accelerate the ARMCO iron flyer plate onto the enclosed rock sample. The preset shock pressure values were modeled using the Hugoniot data for iron and magnetite as described in Fritz et al. (2011). The modeled propagation of the shock and rarefaction waves for a nominal shock pressure of 30 GPa is illustrated in Fig. 1c. The flyer plate impacts the cover plate and from the point of impact (A) a shock wave travels through the cover plate of the container, into the sample and into the main body of the container. The shock wave is then reflected back as a rarefaction wave (B) releasing the shock compressed material to ambient pressures. At (C), the shock front reaches the cover plate at the sample interface, and at (D), the rarefaction

wave releases the shock compressed sample to ambient pressures. Note that using rather thick (~1.3 mm) and dense samples provide optimal conditions for two shock reflections and therefore, for a good estimation of shock pressures within the target volume (Fritz et al. 2011).

However, strong impedance differences between phases can lead to a heterogeneous distribution of peak shock pressures and postshock heating, as a result of strong pressure increases through reflections from high density phases to lower density phases, for example, from metals to silicates (Moreau et al. 2018). While part of the fractured sample can be readily recovered from the container, part of the sample is intimately bonded to it (Fig. 1d), suggesting a possible sample contamination from the container. We want to note that the actual pressure in our sample may deviate from the nominal 30 GPa pressure due to (1) impedance contrast between ARMCO iron and the magnetite-quartz ore, and (2) between individual mineral grains and pores within the rock. This difference may even reach a factor of two (e.g., Langenhorst and Hornemann 2005; Moreau et al. 2018).

After shock experiments, powdered and crushed ore fragments were carefully removed from the Armco iron holder (Fig. 1d). For preparation of polished sections, the material was embedded into epoxy resin and bonded to a glass holder.

Reflected light microscopy was carried out on a Leitz polarization microscope.

A JEOL JXA-8530F field emission microanalyzer was used for electron probe microanalysis (EPMA) combined with backscattered electron (BSE) imaging on the polished sections. The qualitative line scans and local compositions in this study were analyzed with 15 kV acceleration voltage and 50 nA probe current, while for element mapping, 10 kV and 50 nA were used. For the quantitative elemental analysis, ZAF correction was used. Standards for each element were for Fe: pure elemental standard, O: ZrO_2. Si: Wollastonite ($CaSiO_3$), Al: Al_2O_3, Mn: $MnTiO_3$, and Mg: MgO. Some of the images were taken with a Tescan Vega electron microscope at 15 kV.

Micro focussed X-ray diffraction (μ-XRD) was carried out at Sul-X beamline of the ANKA synchrotron radiation source at KIT at a wavelength of 0.88650 Å. The area of interest was selected using a light microscope. Backscattered diffraction patterns were recorded from areas of 50 × 50 μm. XRD pattern were analyzed with the EVA program (AXS, Bruker, Karlsruhe, Germany) using the ICDD PDF2/PDF4 reference database.

Magnetic force microscopy was carried out on a dimension icon microscope (Bruker, Karlsruhe, Germany) equipped with a PPP-MFMR-10 cantilever (Nanosensors, Switzerland).
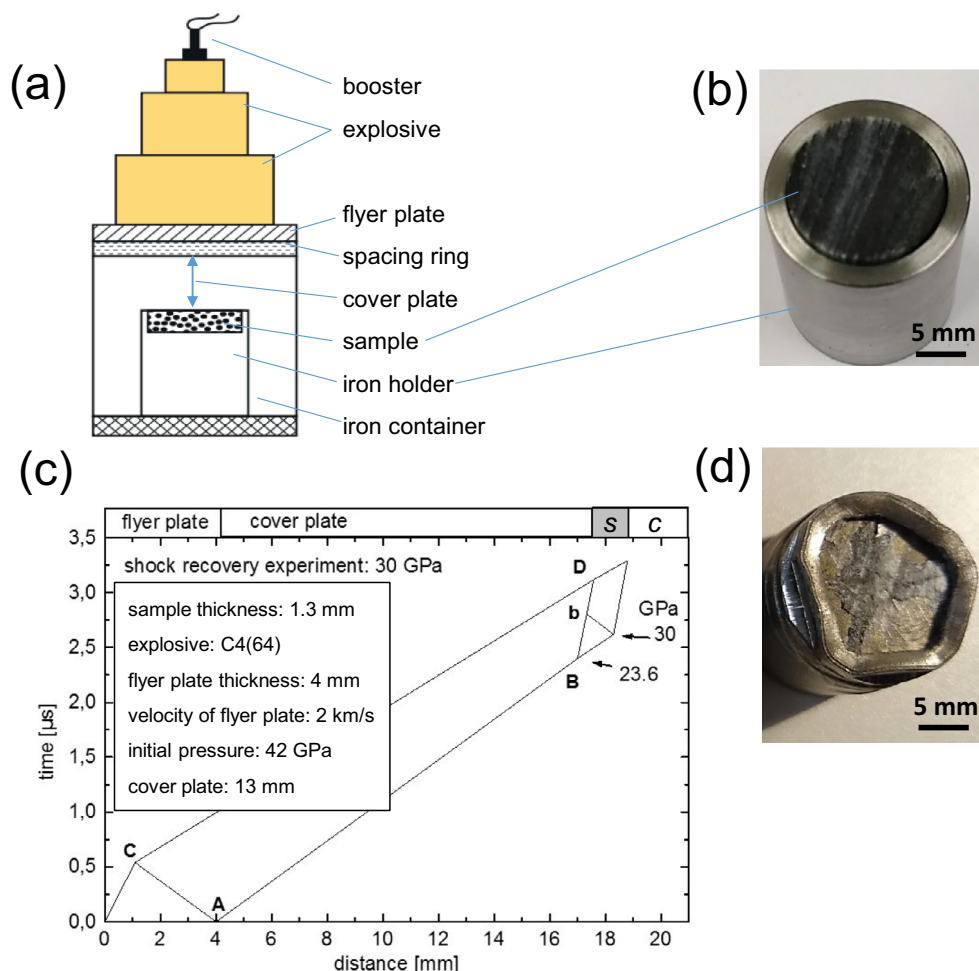
Fig. 1. Shock reverberation experiment. a) Schematic cross section of the high-explosive setup composed of high-impedance ARMCO iron container with the low-impedance rock sample located below the cover plate. b) Iron holder with a specimen before experiment. c) A time versus distance diagram modeled for 30 GPa illustrates propagation of shock from A to B, C, and D. Inset: Experimental conditions (see more details in text). (d) Iron holder showing the contact zone between ore and iron after the 30 GPa shock experiment, and after removal of powdered ore material. (Color figure can be viewed at wileyonlinelibrary. com.)

RESULTS

Figure 2 shows light microscope images of the magnetite ore before (Fig. 2a) and after shock-recovery experiments carried out at 10 (Fig. 2b) and 30 GPa (Fig. 2c).

The unshocked banded magnetite-quartz ore is characterized by magnetite-rich layers alternating with quartz-rich layers (Fig. 2a).

In the loose, shocked material banding is destroyed and some areas contain a number of bright grains (see white arrows in Figs. 2b and 2c) with a very prominent reflectance, higher than that of pyrite, suggesting the appearance of elemental iron. A higher abundance of such grains was observed in the 30 GPa sample. Therefore, this sample was investigated in detail by a combination of different microstructure-sensitive methods at different spatial levels.

Figure 3 presents results of μ-XRD using synchrotron radiation. The XRD pattern from the highly reflective grain (Fig. 2c) contains strong peaks of α-iron and traces of magnetite, quartz, and fayalite (Fig. 3a). The area next to the iron grain (Fig. 3b) represents a mixture of magnetite, fayalite, wüstite, and iron. To validate the presence of fayalite, this area as well as similar intermixed areas were analyzed using SEM in BSE imaging mode combined with EPMA.

Figure 4 shows a BSE image combined with elemental mapping of the area shown in Fig. 3. BSE imaging is very sensitive to the average atomic number z, which is in our case dominated by the Fe content of a given phase. A comparison to EPMA mapping allows
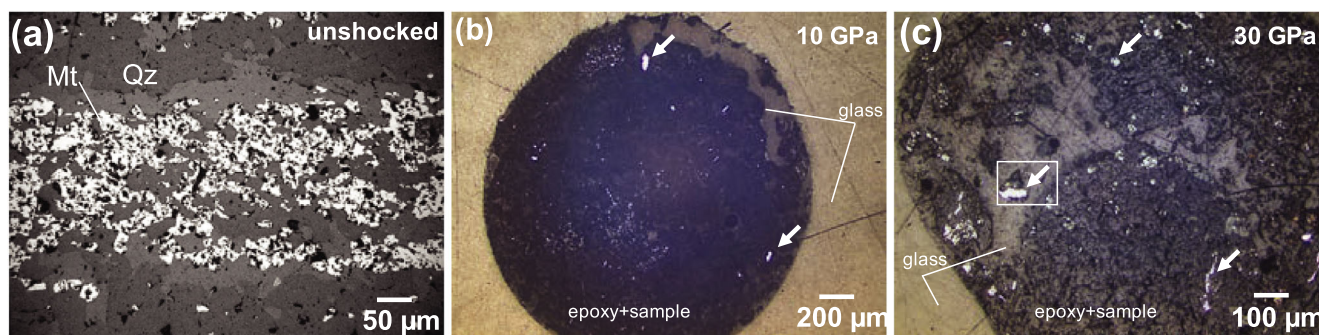
Fig. 2. Reflected light microscopy of magnetite-quartz target ore before and after shock-recovery experiments. a) Quartz- (Qz) and magnetite- (Mt) rich bands characterize the initial sample. b, c) Shocked samples contain injected Fe grains of the ARMCO iron container (white arrows) with high reflectance. The frame in (c) labels the area studied in detail by μ-XRD and EPMA (see Figs. 3–6). (Color figure can be viewed at wileyonlinelibrary.com.)
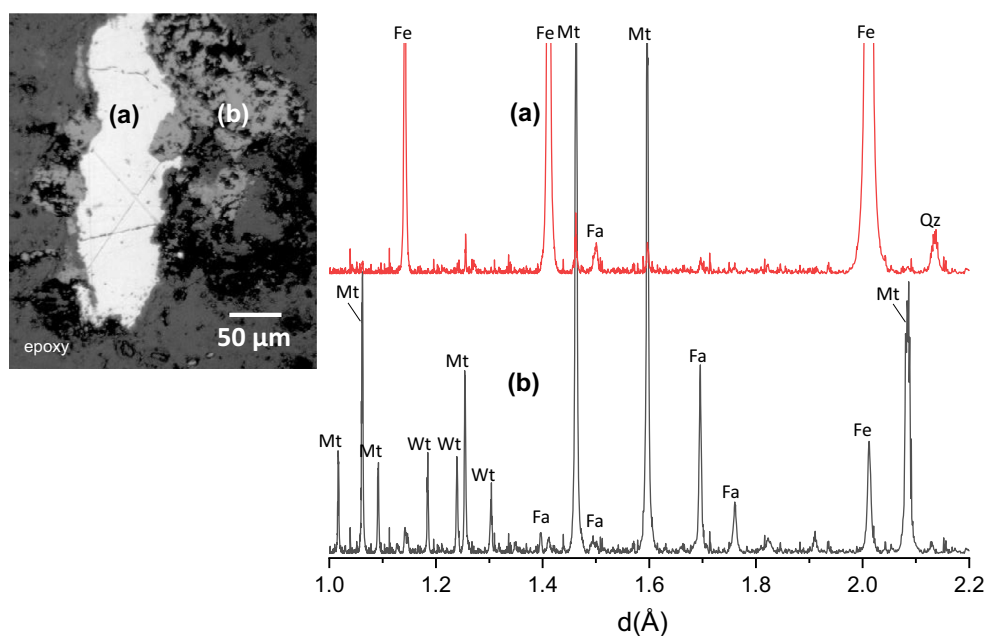

Fig. 3. Reflected light microscope image (left) and micro focussed X-ray diffraction patterns (right) collected from the sample shocked at 30 GPa. a) Iron peaks from the grain exhibiting enhanced reflectance in the optical image; (b) magnetite (Mt), wüstite (Wt), and fayalite (Fa) peaks from the area lying next to the iron-rich grain. (Color figure can be viewed at wileyonlinelibrary.com.)

accurate identification of different phases by BSE imaging. The contrast of BSE imaging indicates that iron is relatively homogeneous, while magnetite and quartz are not (Fig. 4a). In fact, the corresponding mapping of Fe, O, and Si confirms a mottled texture in magnetite and quartz (Figs. 4b–d), which can be related to grain fragmentation but also to chemical variation. The region at the left edge of the iron grain also appears to be inhomogeneous in elemental mapping. We suspect that the iron grain is not very deep in that region so that EPMA due to the excitation volume also probes magnetite below the iron. This becomes

obvious when looking at the SEM-BSE image in Fig. 4a, which is more surface sensitive than EPMA and thus shows a continuous iron grain. Note that the chemical variation acquired by elemental mapping (scale comparable with the scale of light microscope image in Fig. 3) correlates well with the μ-XRD data indicating the formation of shock-induced phases like fayalite, wüstite, and iron.

Figure 5 presents microstructural observations with a higher spatial resolution than in Fig. 4. The well-developed image contrasts allow us to recognize wüstite in the form of narrow rims of up to several μm at the
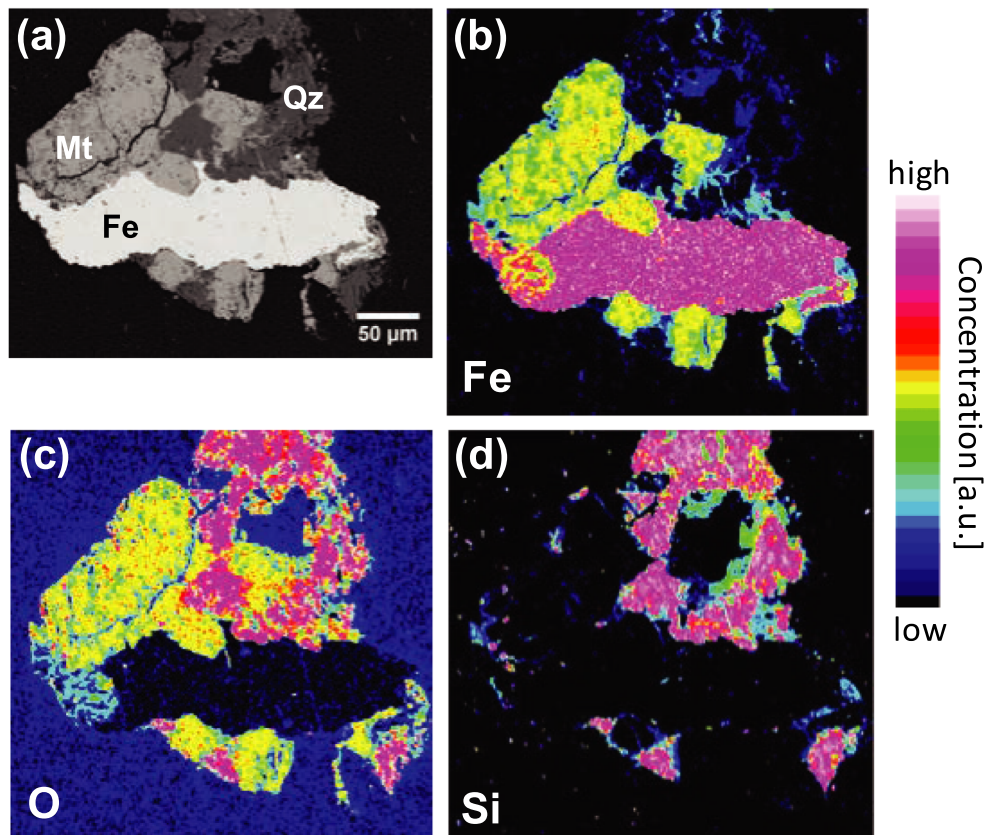
Fig. 4. Elemental mapping of the aggregate shown in Figs. 2c and 3a, 3b. a) Backscattered image shows intergrowth of magnetite (Mt), quartz (Qz), and iron (Fe). b, c, and d) are elemental Fe, O, and Si mapping images, respectively. Note the chemical heterogeneity in Mt- and Qz-rich grain. (Color figure can be viewed at wileyonlinelibrary.com.)

edges of magnetite grains (Fig. 5a). The occurrence of pale gray fayalite-containing areas is supported by EPMA quantitative analysis (see points 1–5 in Fig. 5b and data given in Table 1). Iron and fayalite occur along shock veins and melt pockets within the old magnetite-quartz aggregates (Figs. 5c and 5d). Vesicular dendrites of fayalite are intergrown with single droplets of iron, which coalesce to larger aggregates if their amount is large enough. Fayalite and minor iron droplets also occur along fractures in quartz (Fig. 5e) and sometimes in hornblende (Fig. 5f). The rims of old quartz and magnetite grains often show corrosion surfaces due to melt-crystal reactions. Rarely, silicate-rich droplets were observed in iron (Fig. 5a).

Figure 6a shows an SEM image of a magnetite-wüstite-iron interface. Between wüstite and iron a small rim can be observed, which is not present between magnetite and wüstite. The EPMA elemental maps of Fe and O (Figs. 6b and 6c) as well as the line profile across the interface (Fig. 6d) confirm the occurrence of the three phases. A transition from magnetite over wüstite to elemental iron clearly suggests a gradient in redox conditions during the shock-recovery experiment.

The reducing environment during the shock experiment is also indicated by the intergrowth of elemental iron, fayalite, and wüstite in the center of Fig. 5b.

EPMA shows that magnetite (Fe_3O_4) and wüstite (FeO) are stoichiometric minerals with traces of MnO, SiO_2, and Al_2O_3 (Table 1). The iron is also pure iron with traces of O, Mn, Cr, and Si (Table 2). For comparison, the iron from the ARMCO iron container (see Fig. 1) was also analyzed. The trace elements of both irons are nearly identical, but the concentration of O is higher in the iron from the sample and Mn is higher in the ARMCO iron. The difference is, however, very minor and both are very pure. The composition of the Fe-oxides and of iron was very homogeneous across the whole sample and was determined as arithmetic average of five to ten different analyses for each phase. The standard deviations of these measurements are very small (Tables 1 and 2).

In the case of fayalite, Fe and Si were found as major elements. However, we measured a large variation in these two elements and their oxides (Table 1). This is probably due to the very vesicular texture and the intimate intergrowth of fayalite with quartz, iron, and
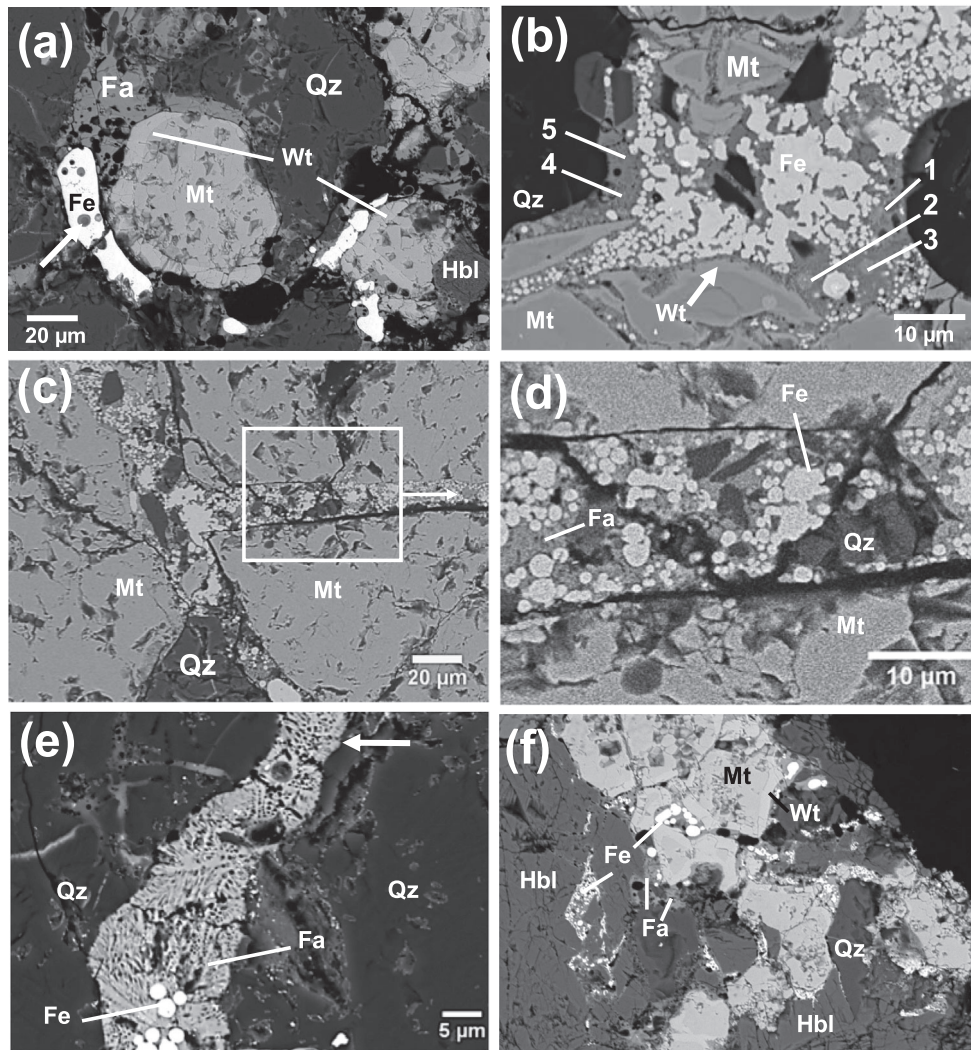
Fig. 5. Backscattered electron images of representative phases. a) Wüstite as rims around magnetite cores (see white bars). Arrow indicates silicate-rich droplets in iron. b) Intermixed regions contain iron and fayalite (points 1–5) determined by EPMA analysis (see Table 1). c and d) show fractured magnetite grains containing veins with fayalite and droplet-shaped iron grains. d) is a close-up of the frame in (c). e) A vein in quartz filled with vesicular dendrites of fayalite, and iron droplets. Note the tiny iron grains in fayalite, which occur in small fractures in quartz. f) Hornblende (Hbl) with iron grains along cleavage planes and microfractures, surrounded by fayalite. For abbreviations, see Figs. 3 and 4.

wüstite (see Fig. 5). It is likely that the large variation represents some amount of Fe-rich silicate melt. Low concentrations of Mg and Ca indicate that hornblende (see e.g., Fig. 5a) may also be involved in the shock melt–induced chemical reactions.

Figure 6e shows a magnetic force microscope (MFM) image with pronounced magnetic domains in magnetite. The magnetic intensity in magnetite is about 10–20 times larger than in the weakly magnetic iron. Wüstite in between the two magnetic phases shows no magnetic domains at all and is paramagnetic. Iron, which has been identified by µ-XRD as α-iron, shows weakly developed irregular, curve-shaped magnetic domains. Normally α-iron is characterized by

a well-developed striped-shaped magnetic domain structure (e.g., Guo et al. 2016).

DISCUSSION

Microstructural observations, µ-XRD as well as EPMA analyses on a magnetite-quartz ore shocked at 30 GPa in an ARMCO iron container clearly show impact-induced features of projectile–target interactions including formation of wüstite and fayalite, and the occurrence of iron from the ARMCO iron container intermingled with the target material (Figs. 1–6). It is evident that fayalite and iron are formed from shock-induced melt(s) (Fig. 5), but their origin is different.

Table 1. Electron probe microanalysis for magnetite, wüstite, and fayalite.

	Magnetite (n = 5)	SD	Wüstite (n = 5)	SD	Fayalite 1	2	3	4	5
SiO_2	0.10	0.05	0.07	0.05	20.82	19.06	20.16	23.33	25.68
Al_2O_3	0.04	0.01	0.05	0.01	0.58	0.57	0.61	0.58	0.57
Fe_2O_3	68.78		0.00		19.22	23.36	21.24	12.91	8.34
FeO	30.85	0.31	98.23	0.26	56.41	53.89	55.70	59.47	62.17
MnO	0.12	0.02	0.10	0.02	0.11	0.14	0.14	0.12	0.11
MgO	n.d.		n.d.		1.01	1.07	1.04	1.10	1.47
CaO	n.d.		n.d.		0.41	0.43	0.39	0.36	0.52
Sum	99.79		98.38		98.56	98.52	99.28	97.86	98.87
Si	0.00		0.00		0.73	0.68	0.71	0.82	0.88
Al	0.00		0.00		0.02	0.02	0.03	0.02	0.02
Fe^{3+}	2.00		0.00		0.51	0.62	0.56	0.34	0.22
Fe^{2+}	1.00		1.00		1.66	1.60	1.63	1.74	1.78
Mn	0.00		0.00		0.00	0.00	0.00	0.00	0.00
Mg	n.d.		n.d.		0.05	0.06	0.05	0.06	0.08
Ca	n.d.		n.d.		0.02	0.02	0.01	0.01	0.02
Sum	3.00		1.00		3.00	3.00	3.00	3.00	3.00

Locations for measurements of magnetite and wüstite were selected randomly across the whole sample and average (avg) and standard deviation (SD) are given for numbers of analyses (n) in wt% oxides. n.d., not detected. For fayalite, single analyses 1–5 are given for points shown in Fig. 5b. Formulas are calculated according to stoichiometry on basis of 4 oxygen (magnetite and fayalite) and 1 oxygen (wüstite).
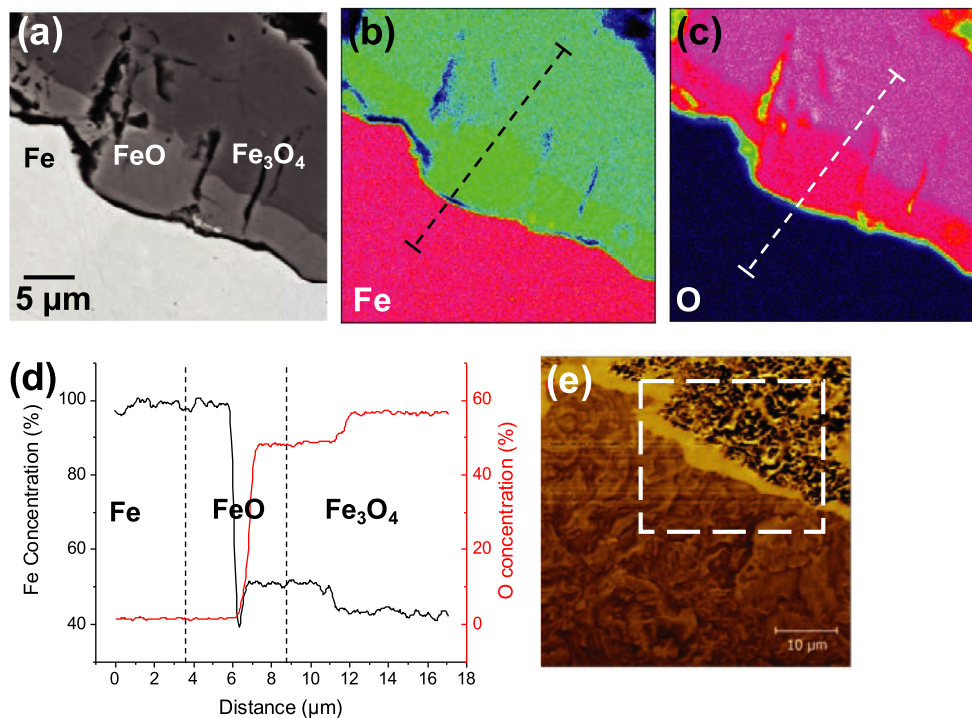Detection limits: SiO_2, Al_2O_3, MgO, CaO = 0.01 wt%, FeO, MnO: 0.02.

Fig. 6. Relationship between chemical and magnetic contrast. a) BSE image of an iron (Fe)-wüstite (FeO)-magnetite (Fe_3O_4) interface; (b and c) are Fe and O mapping from (a) and the scan along dashed line in (b) and (c) is shown in (d). e) MFM image of a larger region (white frame indicates [a]). Note the absence of magnetic domains within wüstite, the weak magnetic domains in iron, and the strong ones in magnetite. (Color figure can be viewed at wileyonlinelibrary.com.)

While iron is a melting product from the ARMCO iron container, fayalite has most likely crystallized from an iron-enriched silicate melt. The concentration of iron droplets and up to several hundreds of μm large aggregates of iron in the sample (Fig. 2) compared to the little amount of fayalite is a strong indication for a

Table 2. Results of electron probe microanalysis for iron from sample and ARMCO iron container. Average (avg) and standard deviation (sd) are given for numbers of analyses (n) in wt% elements.

	Iron in sample		ARMCO iron	
	avg	SD	avg	SD
n	10		5	
O	0.42	0.03	0.13	0.03
Mg	0.00	0.01	0.00	0.00
Fe	100.66	0.29	100.18	0.16
Cr	0.02	0.01	0.03	0.01
Ti	0.00	0.00	0.00	0.01
Mn	0.04	0.01	0.10	0.02
V	0.01	0.01	0.01	0.01
Si	0.03	0.01	0.02	0.01
Al	0.00	0.00	0.00	0.00
Sum	101.19	0.27	100.46	0.18

Detection limits: O = 0.05, Fe, Mn = 0.02, all other elements = 0.01 wt%.

projectile–rock interaction mechanism with melting of the ARMCO iron container. Corrosion of the ARMCO iron container around the sample further supports container–rock interactions (Fig. 1d).
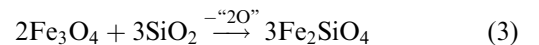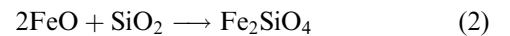
The melt textures suggest that they are products of decompression melts, which are intruded into the fractured magnetite and quartz grains after peak shock conditions. Similar injection and dissemination of iron projectile melt into the target-derived silicate melts were also reported for low shock-recovery experiments in the 10 GPa range from MEMIN (Multidisciplinary Experimental and Modelling Impact Research Network) experiments (e.g., Kowitz et al. 2013; Ebert et al. 2018). From numerical modeling, iron melting at such low shock pressures is reported to occur either due to a strong shock wave concentration effect or due to heating by pore crushing (e.g., Moreau et al. 2018). While the latter effect might hold for the dry and porous sandstone of the MEMIN experiments by Kowitz et al. (2013) and Ebert et al. (2018), our magnetite-quartz ore is a very dense material with low porosity. Therefore, we assume that the iron melt formation only occurs near the contact between target material and surrounding ARMCO iron container (see Figs. 1b and 1d), where a strong impedance contrast between magnetite-quartz ore and iron leads to very high peak temperatures during the shock experiment.

Our observations represent a specific kind of projectile–rock interaction with relevance for asteroid collision or iron meteorite impacts on the Earth. An impact of iron meteorite on sandstone at Henbury, Australia, is described to form submicrometer-sized fayalite, magnetite, quartz, hercynite, diamond, and

Ni-sulfide phase in addition to abundant glass (Ding and Veblen 2004). The impactite is chemically very inhomogeneous presumably because of the immiscibility of metal and silicate melt and the limited diffusion time available for mixing of iron and silica during the rapid cooling history. Ding and Veblen (2004) interpreted the existence of fayalite and magnetite as products of metastable crystallization under supercooled reduced conditions. In the case of our study, the oxygen fugacity is not near the fayalite-magnetite-quartz buffer as described for the Henbury impactites (Ding and Veblen 2004) but near the wüstite-iron buffer indicating much stronger reducing conditions. This observation underlines the significant role of ARMCO iron for the observed textures.

Fayalite was observed as a reaction product at quartz–magnetite interfaces or where magnetite and quartz are in close contact. In Fig. 5, spherules of iron occur in a matrix of fayalite, and coalesce to larger aggregates if their amount is large enough. The common occurrence of (ARMCO) iron droplets, quartz, and fayalite suggests that fayalite crystallized from an Fe-rich silicate melt.

Wüstite always forms a reaction front around magnetite (Fig. 6a) and a solid-state diffusion process due to a strong redox gradient seems to be more likely than a melt origin. The side of wüstite toward iron is characterized by a melt corrosion surface and a small gap, which is understandable in view of an iron melt fusion. The iron droplets and the dendrite-like texture of fayalite (Fig. 5) clearly indicate a rapid cooling from a shock melt. This is also confirmed by the vesicular texture of fayalite. The reduced mineral assemblage indicates conditions during the shock experiment where Fe^{3+} from magnetite was clearly reduced to Fe^{2+} to form wüstite. In the following, different redox reactions for the formation of wüstite and fayalite under consideration of the observed textures are suggested:

$$Fe_3O_4 \xrightarrow{-\text{"O"}} 3FeO \tag{1}$$

$$2FeO + SiO_2 \longrightarrow Fe_2SiO_4 \tag{2}$$

$$2Fe_3O_4 + 3SiO_2 \xrightarrow{-\text{"2O"}} 3Fe_2SiO_4 \tag{3}$$

$$2Fe + SiO_2 \xrightarrow{+\text{"2O"}} Fe_2SiO_4 \tag{4}$$

The reduction Reaction 1 is crucial for the formation of wüstite, which likely reacts with quartz to form an Fe-rich silicate melt (Reaction 2). In contact with quartz even magnetite can form an Fe-rich silicate melt (Reaction 3) from which fayalite can crystallize.

Probably the most conclusive explanation for the occurrence of fayalite is that the ARMCO iron reacts with quartz to form a fayalite melt (Reaction 4) in an oxidation reaction. Melt corrosion rims around quartz and magnetite rimmed by wüstite is ubiquitous (Figs. 5a and 6a) and might favor such an interpretation. This observation suggests that a strongly reduced iron melt travels at high speed through the fractured quartz and magnetite and corrodes the fragments producing a silicate melt, from which fayalite is formed. Silicate-rich melt droplets are rarely observed in iron (Fig. 5a) confirming an emulsification of immiscible and structurally incompatible metal and silicate melts as described, for example, by Hamann et al. (2018). We have not seen immiscibilities between different silicate melts as described in Hamann et al. (2018 and references therein), which is likely due to the low oxygen fugacity during the melt formation in our shock experiment.

It remains unclear what chemical species oxygen is removed from the chemical equations 1–3. One possibility is that oxygen gets oxidized and is released in the form of gaseous O_2. Such a reaction might be understood in terms of an entropy-driven reaction, which becomes possible at high temperatures during or right after the impact. In order to overcome the highly negative formation enthalpy of Fe oxides by an increase in entropy, a very high temperature would be necessary. It might be possible that such high temperatures are reached in certain parts of the sample, because the impact results in a strongly inhomogeneous temperature increase in the sample with extreme local conditions. This is in line with the fact that only a low amount of elemental iron occurs in certain regions of the sample. In this scenario, we would expect to find round pores from O_2 gas inclusions close to iron grains. In fact, round pores in fayalite occur (Fig. 5e), indicating that gaseous O_2 might have developed during the reaction.

ARMCO iron is strongly magnetic and contamination in the samples normally can be easily detected by magnetic methods (see e.g., Mang et al. 2013). The elemental iron seen in the 30 GPa sample from this study shows only weakly developed magnetic domain structures. In the case of α-iron, we would expect a much higher magnetic intensity and well-pronounced magnetic stripe-shaped domains (e.g., Guo et al. 2016). Austenite (γ-iron), the high-temperature modification of α-iron, is paramagnetic (e.g., Tarasov and Parker 1939) and does not show any magnetic domains (e.g., Guo et al. 2016). From our textural observations, it is very likely that γ-iron crystallized at high temperatures due to rapid cooling during the shock experiment from an iron melt (melting point of iron is 1538 °C). The very weak magnetic intensity of the iron

might be a result of an incomplete metastable transformation from the high temperature paramagnetic to a weak magnetic low-temperature modification. In our earlier magnetic studies on this material (Reznik et al. 2016a, 2016b), we have only detected a Curie temperature for magnetite at 580 °C but not for ferromagnetic iron at 780 °C, which underlines the weak magnetic character of the iron. We also have to note that the finding of wüstite-iron-fayalite phases is only a local feature, which is inhomogeneously distributed throughout the shocked material.

The formation of wüstite from magnetite requires at least temperatures of about 1200 °C if γ-iron has formed (and about 850 °C for α-iron; Young 2015). The melting temperature of iron is above 1535 °C (Holleman et al. 2007). Fayalite would also be liquid at this temperature, since its melting point is 1205 °C (Verdes et al. 2012). Magnetite and quartz have higher melting temperatures of ~1600 and ~1670 °C, respectively, than iron depending on conditions like oxygen partial pressure (Deer et al. 1997). Therefore, our shock-recovery experiments at 30 GPa show that during the experiment temperature peaks between about 1200 and 1600 °C occur locally in the sample. This estimate correlates well with our previous observations of foamy textures in hornblende and droplet-shaped nanograins on shear planes in magnetite at 20–30 GPa (Reznik et al. 2016b).

As fayalite transforms to a spinel structure above 6 GPa and to a mixture of wüstite and stishovite (SiO_2) above 22 GPa (Williams et al. [1990] and references therein), we can assume that in our experiment, a decompression melt formed, from which the fayalite crystallized. We have not identified any high-pressure phases in this study. Fayalite, wüstite, and iron are analyzed as polycrystalline, well-crystallized phases (Fig. 3). Previous XRD data of the quartz from the 30 GPa sample show small, broadened diffraction peaks indicating that quartz is not fully amorphous, but strongly deformed (Reznik et al. 2016a).

Fayalite with iron nanoparticles are reported from space weathering (darkening of planetary and asteroidal surfaces) due to micrometeorite impacts or irradiation by the solar wind, for example, on the Moon (Sasaki et al. 2001; Gu et al. 2018). The space weathering effects are amorphization on the surface of soil grains and the formation of nanophase iron particles within the partly amorphous rims showing vesicular textures. It is reported that fayalite decomposes due to the high shock pressure and temperature into nanophase iron and SiO_2 (stishovite). This mechanism is clearly different to what we see in our experiment as no amorphous phase and no high-pressure phase of olivine were observed and our reaction seems to be vice versa

(formation of fayalite from quartz and Fe or Fe-oxide). However, we cannot unequivocally rule out back transformation of various high-pressure phases, since this would require transmission electron microscopy investigations on the quartz-magnetite-wüstite-fayalite-iron interfaces. Only high-resolution methods could resolve such nanophase features (see, e.g., Sasaki et al. 2001; Agarwal et al. 2016; Gu et al. 2018).

CONCLUSIONS

In this study, we reported on a specific kind of geochemical projectile–rock interaction between quartz-magnetite ore and ARMCO iron container, and presented phase transformations from magnetite to wüstite and crystallization of fayalite from an Fe-rich silicate melt. We summarize our findings as follows:

1 After applying 30 GPa shock waves in an experiment, the magnetite-quartz ore reacts with the ARMCO iron container, which intruded as metal melt into fractures of magnetite and quartz, triggering the reduction of magnetite (Fe_3O_4) to wüstite (FeO), and caused melt corrosion at the rims of the intensively fractured target mineral grains.

2 Fayalite (Fe_2SiO_4) has crystallized as vesicular dendritic grains from an Fe-rich silicate melt, which has formed due to wüstite/magnetite and quartz melting under strongly reducing conditions at the wüstite-iron buffer, or due to the reaction between the injected ARMCO iron melt and quartz.

3 Shape and morphology of magnetic domains in iron are sensitive to high-temperature shock-induced phase transformations.

4 The temperature required for these transformations is estimated between 1200 and 1600 °C, indicating that extreme local temperature spikes during the nominal 30 GPa shock laboratory experiments were reached due to strong impedance contrasts between iron container and target material.

5 Emulsion textures (iron droplets in a fayalite matrix and silicate droplets in iron) indicate immiscibility of the Fe-rich silicate and metal melt in accordance with earlier reports by Hamann et al. (2018).

6 Formation of wüstite and fayalite from magnetite cause a decrease in magnetization as both new formed minerals are paramagnetic. This modification has to be taken into consideration if magnetic properties of magnetite are evaluated from a target that came into contact with an iron meteorite.

In order to prevent container–target interaction during shock experiments, the target can be wrapped in tantalum foils. This should be considered if magnetic properties of experimentally shocked material are investigated.

REFERENCES

Acuna M. H., Connerney J. E. P., Ness N., Lin R. P., Mitchell D., Carlson C. W., McFadden J., Anderson K. A., Reme H., Mazelle C., Vignes D., Wasilewski P., and Cloutier P. 1999. Global distribution of crustal magnetization discovered by the Mars Global Surveyor MAG/ER experiment. *Science* 284:790–793.

Agarwal A., Reznik B., Kontny A., Heissler S., and Schilling F. 2016. Lingunite—A high-pressure plagioclase polymorph at mineral interfaces in doleritic rock of the Lockne impact structure (Sweden). *Science Reports* 6:25991.

Deer W. A., Howie R. A., and Zussman J. 1997. *An introduction to the rock-forming minerals.* London: Longman Scientific & Technical. 696 pp.

Ding Y. and Veblen D. R. 2004. Impactite from Henbury, Australia. *American Mineralogist* 89:961–968.

D'Orazio M., Folco L., Zeoli A., and Cordier C. 2011. Gebel Kamil: The iron meteorite that formed the Kamil crater (Egypt). *Meteoritics & Planetary Science* 48:1179–1196.

Ebert M., Kowitz A., Schmitt R. T., Reimold W. U., Mansfeld U., and Langenhorst F. 2018. Localized shock-induced melting of sandstone at low shock pressures (<17.5 GPa): An experimental study. *Meteoritics & Planetary Science* 53:1633–1643.

Fritz J., Wünnemann K., Reimold W. U., Meyer C., and Hornemann U. 2011. Shock experiments on quartz targets pre-cooled to 77 K. *International Journal of Impact Engineering* 38:440–445. https://doi.org/10.1016/j.ijimpeng.2010.10.014.

Gattacceca J., Lamali A., Rochette P., Boustie M., and Berthe L. 2007. The effects of explosive-driven shocks on the natural remanent magnetization and the magnetic properties of rocks. *Physics of the Earth and Planetary Interiors* 162:85–98.

Gu L., Zhang B., Hu S., Noguchi T., Hidaka H., and Lin Y. 2018. The discovery of silicon oxide nanoparticles in space-weathered of Apollo 15 lunar soil grains. *Icarus* 303:47–52.

Guo L., Hua G., Yang B., Lu H., Qiao L., Yan X., and Li D. 2016. Electron work functions of ferrite and austenite phases in a duplex stainless steel and their adhesive forces with AFM silicon probe. *Scientific Reports* 6:20660. https://doi.org/10.1038/srep20660.

Hamann C., Hecht L., Ebert M., and Wirth R. 2013. Chemical projectile-target interaction and liquid immiscibility in

impact glass from the Wabar craters, Saudi Arabia. *Geochimica et Cosmochimica Acta* 121:291–310.

Hamann C., Fazio A., Ebert M., Hecht L., Wirth R., Folco L., Deutsch A., and Reimold W. U. 2018. Silicate liquid immiscibility in impact melts. *Meteoritics & Planetary Science* 53:1594–1632.

Holleman A. F. E., Wiberg N., and Fischer G. 2007. *Lehrbuch der Anorganischen Chemie*. Berlin: Walter de Gruyter.

Kontny A., Reznik B., Boubnov A., Göttlicher J., and Steininger R. 2018. Postshock thermally induced transformations in experimentally shocked magnetite. *Geochemistry, Geophysics, Geosystems* 19:921–931.

Kowitz A., Schmitt R. T., Reimold W. U., and Hornemann U. 2013. The first MEMIN shock recovery experiments at low shock pressure (5-12.5 GPa) with dry, porous sandstone. *Meteoritics & Planetary Science* 48:99–114.

Langenhorst F. and Hornemann U. 2005. Shock experiments on minerals: Basic physics and techniques. *EMU Notes Mineral* 7:357–387.

Mang C., Kontny A., Fritz J., and Schneider R. 2013. Shock experiments up to 30 GPa and their consequences on microstructures and magnetic properties in pyrrhotite. *Geochemistry, Geophysics, Geosystems* 14:64–85. https://doi.org/10.1029/2012GC004242.

Moreau J. G., Kohout T., and Wünnemann K. 2018. Melting efficiency of troilite-iron assemblages in shock-darkening: Insight from numerical modeling. *Physics of the Earth and Planetary Interiors* 282:25–38.

Pilkington M. and Grieve R. A. F. 1992. The geophysical signature of terrestrial impact craters. *Reviews of Geophysics* 30:161.

Reznik B., Kontny A., Fritz J., and Gerhards U. 2016a. Shock-induced deformation phenomena in magnetite and their consequences on magnetic properties. *Geochemistry, Geophysics, Geosystems* 17:1–20. https://doi.org/10.1002/2016GC006338.

Reznik B., Kontny A., and Fritz J. 2016b. Effect of shock waves on magnetic susceptibility and microstructure of a magnetite-bearing ore. *Meteoritics & Planetary Science* 52:1495–1504. https://doi.org/10.1111/maps.12787.

Sasaki S., Nakamura K., Hamabe Y., Kurahashi E., and Hiroi T. 2001. Production of iron nanoparticles by laser irradiation in a simulation of lunar-like space weathering. *Nature* 410:555–557.

Tarasov L. P. and Parker E. R. 1939. Ferromagnetism in austenite. *Physical Review* 56:379.

Williams Q., Knittle E., Reichlin R., Martin S., and Jeanloz R. 1990. Structural and electronic properties of Fe_2SiO_4-fayalite at ultrahigh pressures: Amorphization and gap closure. *Journal of Geophysical Research* 95:21549.

Verdes B., Chira I., Virgolici M., and Moise V. 2012. Thermal stability of fayalite system formation at the interface between steel and mould. *University Politehnica of Bucharest Science Bulletin, Series B* 74:257–268.

Young D. 2015. *High-temperature oxidation and corrosion of metals*. Amsterdam: Elsevier. 760 pp.